Fusion Engineering and Design 219 (2025) 115215

Contents lists available at ScienceDirect

Fusion Engineering and Design

journal homepage: www.elsevier.com/locate/fusengdes

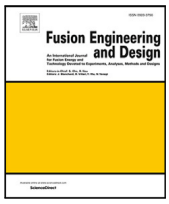

Bubble dynamics in Magnetohydrodynamics conditions: Numerical simulation and flow characterization for high density ratio mixture

Sonia Pignatiello *, Simone Siriano, Alessandro Tassone

Nuclear Engineering Research Group, DIAEE - Sapienza University of Rome, C.so Vittorio Emanuele II 244, 00186 Rm, Rome, Italy

ARTICLE INFO

Keywords:
Volume of Fluid
Bubble dynamics
Liquid metals
MHD
OpenFOAM

ABSTRACT

Many Breeding Blanket (BB) concepts envision the use of a liquid metal (LM) alloy containing lithium to fulfill the functions of tritium production through the tritium breeding reaction, which produces helium as a by-product. This, under appropriate conditions, can nucleate, aggregate into bubbles that can be transported within the main fluid flow. The study of the bubbles transport within the magnetohydrodynamic (MHD) LM flow is mandatory to assess the impact on the BB performance and safety, due to their potential accumulation in some part of the system.

In this study, the dynamics of bubbles in MHD conditions is examined using a custom OpenFOAM solver called `mhdInterFoam` (`mIF`). This code is capable of modeling a two-phase MHD flow of incompressible, immiscible, and isothermal fluids using the Volume of Fluid (VoF) method. The code has been validated against experimental data, producing results in good agreement with the reference for several bubble diameters (Eötvös number, Eo ≈ 1.5 - 8.5) and magnetic fields up to 1.5 T (Hartmann number, Ha ≈ 0 - 220).

Specifically, the magnetic field effects on the bubbles regime of motion are analyzed and the characteristics of the LM flow around the bubbles are presented. The study is performed considering the distribution of fundamental physical quantities, which are challenging to investigate through experimental studies alone.

1. Introduction

One of the central components in the operation of a nuclear fusion reactor for power production will be the Breeding Blanket (BB). Many concepts envision the use of a liquid metal alloy containing lithium as the main working fluid to fulfill the functions of tritium production and heat extraction. During the tritium breeding reaction that is occurring in lithium, helium is produced as a by-product and, under appropriate conditions, it can nucleate and be transported as bubbles within the main fluid stream [1,2]. The transport and behavior of these helium bubbles, and how it is affected by the reactor magnetic field, play a role in determining the component performance and safety since they affect the Tritium Breeding Ratio (TBR), reduce its shielding capabilities and alter LM/wall heat and mass coefficients and local electrical variables [2]. Given the challenges of directly observing the bubbles behavior in liquid metals due to their opaqueness and of obtaining flow and electric variable distribution [3], this study addresses the issue of numerical modeling and predicting the magnetohydrodynamics (MHD) effects on the dynamic of the bubbles in the liquid metal breeder. For this purpose, the `mhdInterFoam` (`mIF`) numerical code has been developed implementing the MHD equations in the OpenFOAM (OF) solver `interIsoFoam` [4–6].

The `mhdInterFoam` is a solver capable of performing MHD transient simulations of two incompressible, isothermal and immiscible fluids employing the Volume of Fluid (VoF) method. Currently, it is possible to model ideal electric wall conditions through BCs, such as perfectly electrically insulated and conductive walls. As mentioned above, the solver is based on the `interIsoFoam` solver of OF v2212, with optional mesh motion and mesh topology changes including adaptive re-meshing. This base code was chosen because it is able to perform hydrodynamic simulations for high-density mixtures, a potentially critical condition for multiphase numerical models. It was tested by the authors for several flow regime for the rise of helium bubbles within the lead–lithium eutectic alloy [7]. The implementation of MHD effects was carried out by adapting the guidelines from what is arguably the most significant work in numerical modeling of MHD multiphase phenomena, the 2014 study by Zhang et al. [8], to the structure of the base solver. The `mIF` code has been already validated by the authors [9] performing simulation of several nitrogen bubbles in liquid mercury under the influence of a transverse uniform magnetic field B_0. This particular case was previously explored by Mori et al. [10], where the bubble dynamics for various initial equivalent diameters d (Eo

* Corresponding author.
E-mail address: sonia.pignatiello@uniroma1.it (S. Pignatiello).

https://doi.org/10.1016/j.fusengdes.2025.115215
Received 18 December 2024; Received in revised form 20 March 2025; Accepted 19 May 2025
Available online 10 June 2025
0920-3796/© 2025 The Authors. Published by Elsevier B.V. This is an open access article under the CC BY license (http://creativecommons.org/licenses/by/4.0/).

Nomenclature

$\mathbf{B}_0$	Magnetic field [T]
$\mathbf{g}$	Gravitational acceleration [m/s^2]
$\mathbf{j}$	Electric current density [A/m^2]
$\mathbf{u}$	Velocity vector [m/s]
Co	Courant number
d	Bubble equivalent diameter [m]
Eo	Eötvös number
Ga	Galilei number
Ha	Hartmann number
N	Interaction parameter
p	Pressure [Pa]
Re	Reynolds number
t_{conv}	Convective characteristic time [s]
t_{surf}	Surface tension characteristic time [s]
t_{visc}	Viscous characteristic time [s]
u	Velocity x-component [m/s]
u_g	Gravitational velocity [m/s]
u_T	Bubble terminal velocity [m/s]
v	Velocity y-component [m/s]
w	Velocity z-component [m/s]
We	Weber number
α	Volume fraction
β	Interpolated material property
Δt	Time-step [s]
Δx	Minimum cell dimension [m]
γ	Surface tension coefficient [N/m]
κ	Interface curvature [1/m]
μ	Dynamic viscosity [Pa s]
ν	Kinematic viscosity [m^2/s]
ρ	Density of the mixture [kg/m^3]
ρ_g	Gas phase density [kg/m^3]
ρ_l	Liquid phase density [kg/m^3]
σ	Electrical conductivity [S/m]
τ_M	Magnetic damping time [s]
φ	Electric potential [V]

$= \rho_l g d^2/\gamma \approx 1.5$–$8.5$) was investigated under three different magnetic field intensities, ranging from 0.5 to 1.5 T (Ha $= dB_0\sqrt{\sigma/(\rho_l \nu)} \approx$ 0–220). The bubble equivalent diameter is used because it is evaluated through the bubble volume measurement, using nitrogen massflow rate, nozzle injection time and considering the bubble with a spherical shape.

Mori and his team conducted the first significant experimental work on bubble motion in MHD conditions. Their study focused on measuring the shape and rise velocities of nitrogen bubbles in mercury using an electrical triple probe. They found that an increase in field intensity stabilizes bubble trajectories while bubble velocity tends to decrease for large bubbles ($d \geq 3.6$ mm). Instead, for small bubbles ($d \leq 2.5$ mm), the tendency is opposite for magnetic field up to 1 T since it prevents the spiral motion, correspondingly allowing an increase of the terminal velocity. Bubbles with an intermediate diameter have a behavior that falls in between that of large and small diameter ones. Other relevant experimental works were carried out using Galinstan alloy (an eutectic mixture of gallium, indium, and tin) as liquid metal and argon bubbles with both, transverse and parallel magnetic field respect to the bubble rising motion [11–14]. In particular Mori et al. [10] work was chosen by the authors for the validation because the measurement techniques used in the experiments with Galistan, Ultrasound Doppler Velocimetry (UDV) and Ultrasound Transit Time (UTT) with X-ray radiography, involve the use of oxides which compromise the measurements results also in hydrodynamic conditions as demonstrated by the discrepancies with Mendelson formula [15] or Tomiyama correlation [16] shown in Refs. [12,13].

As can be observed in Table 1, several numerical codes have been developed to simulate bubble motion in MHD conditions. The only numerical works that carried out simulating nitrogen bubbles in liquid mercury were performed by Zhang & Ni [8] and Jin et al. [17]. The numerical results of the latter two works were used for a code to code comparison with mIF code as can be found in the authors' previous paper [9]. In particular, Zhang & Ni [8] developed an approach for simulating the multi-phase MHD flows on an unstructured Cartesian adaptive system. The approach used in Ref. [8] is based on the VoF method for capturing the interface with the Adaptive Mesh Refinement (AMR) technique used to resolve the interface and the boundary layer. The code developed is in good agreement with Mori experimental result for $d = 5.6$ mm and magnetic field ranging from 0.5 to 1.5 T but a discussion on bubble shapes, trajectories and flow field characteristic are not found for this specific case. The same occurs in Jin et al. [17] work in which several simulations with different liquid metals and gas bubbles were carried out using an in-house numerical code based on Pressure Boundary Method (PBM). In this case the surface tension is modeled as a pressure gradient which perfectly balances the surface tension force generated by the presence of the interface. This new pressure field cannot generate velocity in a static case and gives rise to another pressure Poisson equation. In this way the surface tension force is treated as a jump condition for calculating this new pressure field. The rising velocity profile result for $d = 5.6$ mm and $B_0 = 0.5$ T was used for the validation of mIF code and it has been reported in authors' previous paper [9].

Mori et al. experiments were recreated out for bubbles within the laminar to turbulent transition region in which the bubble dynamic can change widely with varying diameter. To the best of the authors' knowledge, there appear to be no MHD simulations that extensively discuss the magnetic field effects on flow features for this combination of Ha and Eo numbers. Thus, the purpose of this paper is to characterize the bubble dynamics in these MHD conditions describing the interactions between flow and electric fields and their principle effects on trajectories, shapes and wakes. The obtained results are in agreement with Mori et al. [10] experimental findings and with the theoretical discussion and numerical results of Corrado & Sato [18].

The outline of the paper is as follows: in Section 2 the implemented equations and numerical method are presented. In Section 3 the mIF validation is expanded respect to Ref. [9]. The results obtained are analyzed in Section 4 and the influence of the magnetic field on the bubble dynamics is discussed. Finally, conclusions and future works are reported in Section 5.

2. Numerical method

2.1. Governing equations and non-dimensional parameters

This section outlines the assumptions and the implemented equations in the mIF solver. The two phases involved are homogeneous, isotropic, incompressible and immiscible fluids. The Newtonian fluid model is employed and heat transfer and chemical reactions are not considered. The two-phase modeling is realized employing the VoF method, a variant of the more general Eulerian–Eulerian multi-phase model that employs a interface-tracking technique which solves the equation of the phase volume fraction α in each Control Volume (CV) [28]. A value equal to 0 of the scalar function α corresponds to the presence of phase1 in a specific CV whereas a value of 1 corresponds to the presence of phase2. CVs with values between these two extremes represent the interface between the two phases. The use of the volume fraction α allows to solve one single momentum equation for both

Table 1
Experimental and numerical works overview. The symbols E and C stands respectively for Experimental and Computational. With the acronyms HMF and VMF means respectively Horizontal Magnetic Field and Vertical Magnetic Field respect to the bubble flow direction. N/A stands for Not Available.

Year	Author	E/C	Gas, liquid	Field direction	Field strength	Bubble size
1977	Mori et al. [10]	E	N_2 - Hg	HMF	B = 0–1.5 [T]	Eo = 0.88–8.5
1995	Ueno et al. [19]	C	N/A	VMF	N/A	N/A
1999	Ueno et al. [20]	C	N/A	VMF	$\Pi = \mu_0 H_0/\rho_l u_0$ = 0–15	N/A
2005	Zhang et al. [11]	E	Ar-GaInSn	VMF	B = 0–0.3 [T]	Eo = 2.2–6.6
2008	Merrouche et al. [21]	C	N/A-GaInSn	VMF	B = 0–0.15 [T]	Eo = 3.4
2009	Zhang et al. [12]	E	Ar-GaInSn	HMF	B = 0–0.3 [T]	Eo = 2.7–6.9
				VMF		Eo = 2.2–6.6
2010	Shibasaki [22]	C	N/A	VMF	Ha = (0, 25, 50, 75,100, 200)	N/A
2012	Pan and Ni [23]	C	N/A	HMF	Ha = (0, 50)	N/A
2014	Schwarz et al. [24]	C	Ar-GaInSn	VMF	B = 0–2 [T]	Eo = 2.5
2014	Zhang and Ni [8]	C	Ar-GaInSn	VMF	B = 0–0.5 [T]	Eo = 0.74–4.9
			N_2 - Hg	HMF	B = 0–1.5 [T]	d = 5.6 mm
			Ar-GaInSn	VMF	B = 0–0.3 [T]	Eo = 1.2–2.5
2016	Tian et al. [25]	C	N/A	VMF	B = 0–0.4 [T]	d = 4–12 mm
2016	Jin et al. [17]	C	N_2 - Hg	HMF	B = 0–0.54 [T]	d = 5.6 mm
			Ar-Steel			0.51–2.8
2017	Wang et al. [13]	E	Ar-GaInSn	HMF	B = 0–2 [T]	Eo = 1.12–3.67
2018	Richter [14]	E	Ar-GaInSn	HMF	B = 0–0.505 [T]	d = 4.6–6.1 mm
2021	Blishchik [26]	C	N/A	VMF	Ha = (0, 50, 100, 200)	N/A
2021	Flint et al. [27]	C	Ar-GaInSn	HMF	B = 0–0.505 [T]	d = 5.2 mm
2022	Corrado et al. [18]	C	Ar-GaInSn	HMF	B = 0–2 [T]	Eo = 1.12–3.67

phases instead of two as in Eulerian–Eulerian models. Assuming that no phase change occurs, a phase-mass conservation equation is introduced:

$$\frac{\partial \alpha}{\partial t} + \nabla \cdot (\alpha \boldsymbol{u}) = 0 \tag{1}$$

Essentially, Eq. (1) represents the advection equation of the interface whose purpose is to reach a solution that ensure its sharpness. This is realized in two steps using the isoAdvector method [4–6]. First, the interface inside cells is modeled with an iso-surface in a geometric surface reconstruction step. The reconstruction-step is based on the construction of the planar isosurface, called also isoface, inside the CVs located on the interface, so where $0 < \alpha < 1$. To do this, the values stored in the center of the CV are interpolated at its vertices and, from these values, the isoface is calculated at a value of α, specific for the single CV, so that the two generated sub-volumes are proportional to the volume fraction in the specific CV [7]. Then, the isoface motion is estimated within the time-step, in the advance-step, using the velocity data of the surrounding cells and therefore, in practice, evaluating the motion in a sub-time step. The intersection of the isoface with the faces of the CV generates the face-interface intersection line which is used to determine the volume of phase1 transported through the face from which the new distribution of α in the domain is derived [7]. Indeed, the final goal of this numerical procedure is to provide a good estimate of the local fluid distribution in order to properly capture the interface maintaining it sharp.

Once that the α field is evaluated, so that each CV is associated with an α value equal to 0 (presence of phase1 in the CV), or equal to 1 (presence of phase2 in the CV) or between 0 and 1 (phase1/phase2 interface), all the generic material properties (indicated with β) are evaluated with a linear interpolation reported in the formula below:

$$\beta = \alpha\beta_1 + (1-\alpha)\beta_2 \tag{2}$$

This approach allows to solve a single momentum equation for the whole system instead of two, as in Eulerian–Eulerian models, since the material properties used in the equations can vary according to α. The momentum equation implemented in mIF code, which includes the Lorentz force, is reported below:

$$\rho\left[\frac{\partial \boldsymbol{u}}{\partial t} + (\boldsymbol{u}\cdot\nabla)\boldsymbol{u}\right] = -\nabla p + \nabla\cdot\tau + \boldsymbol{F}_S + \rho\boldsymbol{g} + \boldsymbol{F}_L \tag{3}$$

where $\boldsymbol{u}$ is the velocity, p is the pressure, ρ is the density, τ is the viscous stress tensor, $\boldsymbol{g}$ the gravitational acceleration and $\boldsymbol{F}_L$ is the Lorentz force. The surface tension force $\boldsymbol{F}_S$ is modeled as a volumetric force employing the Continuum Surface Force (CSF) technique of Brackbill et al. [29]

$$\boldsymbol{F}_S = \gamma\kappa\nabla\alpha \tag{4}$$

$$\kappa = \nabla\cdot\left(\frac{\nabla\alpha}{|\nabla\alpha|}\right) \tag{5}$$

where γ is the surface tension coefficient and κ the interface curvature. In this way the surface tension force is non-zero only in the interface region, due to the fact that the gradient of α in the surface force calculation act as a Kronecker delta, thus incorporating its effect solely at the interface although it is incorporated into the momentum equation as a volumetric force.

The Lorentz force in the momentum equation is evaluated with the relation below:

$$\boldsymbol{F}_L = \boldsymbol{j}\times\boldsymbol{B_0} \tag{6}$$

where $\boldsymbol{j}$ is the electric current density and $\boldsymbol{B_0}$ is the imposed magnetic field. The implementation of the Lorentz force in mIF was realized using the conservative formulation presented by Ni et al. [30] which guarantees electric current conservation (Eq. (7) below), as deeply discussed in authors' previous paper [9].

$$\nabla\cdot\boldsymbol{j} = 0 \tag{7}$$

For the evaluation of the electric current density, since the liquid phase is a LM, the displacement electric current can be neglected (low-frequency approximation), as well as the accumulation of electric charge (quasi-neutral approximation) and the induced magnetic field (low-magnetic Reynolds approximation). Thus, the electric potential formulation of MHD equations can be used considering the electric potential φ as the main electrical variable [31]. The combination of Navier Stokes's, Maxwell's and Ohm's equations returns the equation system implemented in mIF code:

$$\nabla\cdot\boldsymbol{u} = 0 \tag{8}$$

$$\frac{\partial \alpha}{\partial t} + \nabla\cdot(\alpha\boldsymbol{u}) = 0 \tag{9}$$

$$\rho\left[\frac{\partial \boldsymbol{u}}{\partial t} + (\boldsymbol{u}\cdot\nabla)\boldsymbol{u}\right] = -\nabla p + \rho\nu\nabla^2\boldsymbol{u} + \gamma\kappa\nabla\alpha + \rho\boldsymbol{g} + \boldsymbol{j}\times\boldsymbol{B_0} \tag{10}$$

$$\nabla^2\varphi = \nabla\cdot(\boldsymbol{u}\times\boldsymbol{B_0}) \tag{11}$$

$$\boldsymbol{j} = \sigma(-\nabla\varphi + \boldsymbol{u}\times\boldsymbol{B_0}) \tag{12}$$

where ν is the kinematic viscosity, σ is the electrical conductivity, Eqs. (11) and (12) are respectively the electric potential Poisson equation and Ohm's law. All the material properties are evaluated according to Eq. (2).

The dimensionless parameters which completely describe a magneto-hydraulic bubble flow under the proposed assumptions include: the Reynolds number $\mathrm{Re} = u_T L/\nu$, which represents the ratio between inertial and viscous forces; the Weber number $\mathrm{We} = \rho_l u_T^2 L/\gamma$, which is the ratio between the inertial forces and the surface tension ones; the interaction parameter (or Stuart number) $\mathrm{N} = \sigma {B_0}^2 L/(\rho_l u_T)$, which represents the ratio between electromagnetic and inertial forces, and the Hartmann number $\mathrm{Ha} = \sqrt{\mathrm{NRe}} = LB_0\sqrt{\sigma/(\rho_l \nu)}$ which is the square root of the ratio between electromagnetic and viscous forces. The quantities u_T and L are the bubble terminal velocity and the characteristic length which corresponds to the bubble diameter.

Considering the gravitational velocity $u_g = \sqrt{gL}$ instead of the bubble terminal velocity u_T in Re and We, two relevant parameters for the bubble shape definition can be found: the Galilei number $\mathrm{Ga} = u_g L/\nu$, which is the ratio between the gravitational forces to the viscous ones, and the Eötvös number $\mathrm{Eo} = \rho_l g L^2/\gamma$, that can be seen as the ratio between the gravitational forces and the surface tension ones.

2.2. Code workflow and numerical set-up

In this section, the workflow of the mIF code is briefly described. A comprehensive description of the MHD equations discretization and solution can be found in [9].

The algorithm that the mIF code follows is presented below:

1. Initial mapping of the fields ($\boldsymbol{u}$, p, φ, α) from imposed initial and boundary conditions, evaluation for $t = 0$ of the Lorentz force.
2. The α transport Eq. (9) is solved through the isoAdvector step for interface reconstruction using the $\boldsymbol{u}^{t-1}$ field evaluated at the previous time-step (which corresponds to $t = 0$ for the first time-step).
3. Material properties are updated with the new α^t field with Eq. (2).
4. PIMPLE[1] algorithm for velocity–pressure coupling at time t is executed (nCorrectors).
5. Solving of the electric potential Poisson Eq. (11) for φ.
6. Calculation of the φ gradient and solving of Ohm's law Eq. (12).
7. Evaluation of the updated value of the Lorentz force.
8. Performing of eventual n external PIMPLE loops (nOuterCorrectors) to improve the coupling between the dynamic and electromagnetic variables and in general the stability, repeating the procedure from 4 to 7.
9. Repeat steps from 2 to 7 or 8 for $t = t + dT$ using the obtained variable values at the end of step 7 or 8.

3. Numerical model and validation

This section briefly expands on the validation of mIF [9]. The validation consist in simulating a nitrogen bubble rising in a square channel filled with liquid mercury in hydrodynamic (HYDRO) conditions and under a constant transverse magnetic field $\boldsymbol{B_0}$ with intensity ranging from 0.5 to 1.5 T.

This case was experimentally explored by Mori et al. [10], for the same magnetic field intensities and different bubble equivalent diameters d and numerically by Zhang & Ni [8] only for the largest bubble diameter and equal magnetic fields. The bubble terminal velocity value u_T is the main validation parameter and velocity trends are only available from numerical studies.

[1] Pressure Implicit Method for Pressure-Linked Equations.

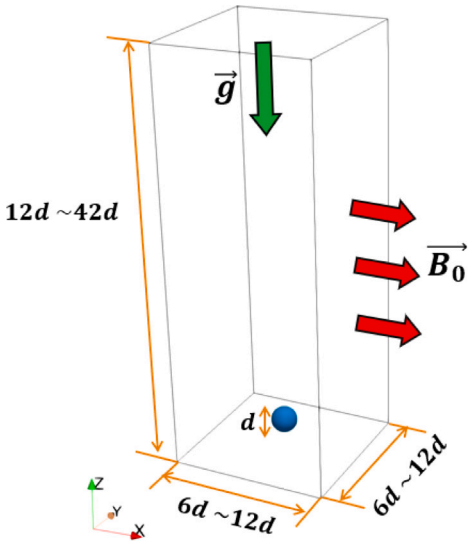

Fig. 1. Computational domain based on bubble equivalent diameter and initial simulation setup.

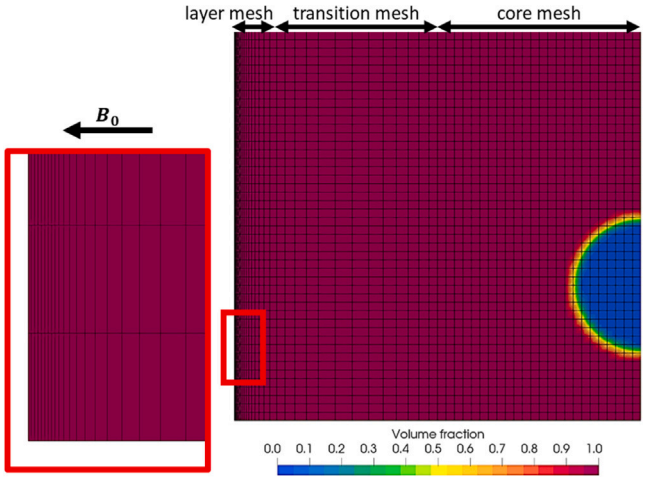

Fig. 2. Computational grid on the bottom part of the midplane cross–section for the bubble with $d = 5.6$ mm and $B_0 = 0.5$ T at time zero. Detail of the nodes distribution through the Hartmann layer (left box).

The numerical domain, in Fig. 1 is a parallelepiped, with a square base whose dimensions change according to the bubble equivalent diameter d, velocity and the flow conditions (HYDRO and MHD). For the HYDRO cases the domain has a square base that varies from $6d \times 6d$ to $12d \times 12d$ due to bubble trajectory and a height ranging from $32d$ to $42d$ while for the MHD case the square base is fixed at $6d \times 6d$ and the height varies from $16d$ to $32d$.

The bubble volume is initialized imposing $\alpha = 0$ at $t = 0$ in a spherical volume with d as diameter, in the center of the square base, with a distance from the bottom wall of $1d$ (referred to its centroid) as can be seen from Figs. 1 and 2. A zero-velocity initial condition is applied throughout the domain for both phases. The physical properties used in all the simulations are summarized in Table 3. Regarding the boundary conditions, the no-slip condition for velocity and the zeroGradient condition for pressure, volume fraction and electric potential ($\nabla p \cdot \mathbf{n}$, $\nabla \alpha \cdot \mathbf{n}$ and $\nabla \varphi \cdot \mathbf{n}$) have been applied on all walls. This last condition is in agreement with the glass insulating walls employed in the experiment of Mori et al. [10].

Generating an appropriate computational grid that balances accuracy with computational efficiency is challenging when modeling

Table 2
Summary of the computational domain dimensions, core region cell size and total grid elements of all the simulations performed.

B_0 (T)	d (mm)	Domain dimensions (mm)	Core region cell size (mm)	Mesh elements
0.0	2.36	28.32 × 28.32 × 99.12	0.1475	15 116 544
0.0	3.87	30.96 × 30.96 × 139.32	0.2428	4 478 976
0.0	5.60	33.6 × 33.6 × 179.2	0.35	3 442 688
0.5	2.36	14.16 × 14.16 × 75.52	0.1475	6 889 472
0.5	3.87	23.22 × 23.22 × 98.88	0.2428	5 622 144
0.5	5.60	33.6 × 33.6 × 89.6	0.35	4 064 256
1.0	2.36	14.16 × 14.16 × 75.52	0.0983	17 743 872
1.0	5.60	33.6 × 33.6 × 89.6	0.23	9 953 664
1.5	2.36	14.16 × 14.16 × 56.64	0.0983	14 017 536
1.5	5.60	33.6 × 33.6 × 62.7	0.23	7 936 128

such flows. The presence of nitrogen, an effective electrical insulator, causes MHD layers to form near the interface, requiring a highly refined mesh in all parts of the domain where the bubble ascends to capture these layers. This necessitates either a large number of mesh elements or the use of Adaptive Mesh Refinement (AMR) techniques to automatically refine the mesh near the interface. While the mIF solver can utilize AMR from the interIsoFoam solver, applying it to MHD cases has proven difficult, with previous attempts yielding unsatisfactory results. Notably, an inherent issue arises when utilizing the Crank–Nicolson scheme with AMR for temporal discretization, as the simulation fails to restart once stopped. In an effort to address this issue, two alternative time discretization schemes were explored: the Euler scheme and the backward scheme. The conducted simulations, with both schemes, revealed the propagation of numerical errors, mostly at the interface, leading to an automatic and significant increase in the computational grid. This phenomenon may potentially be mitigated by reducing the time-step. Consequently, the adopted meshing strategy does not take into account the resolution of the MHD layers near the interface. Indeed, the authors estimated that using a uniform mesh in the region traveled by the bubble and considering at least two grid nodes in the MHD boundary layer, the computational grid would entail an unfeasible cost since it would amount to a number of elements varying from 88 millions to 1 billion, depending on the Ha number. The computational time required to solve these meshes would have been years with the resources available to the authors. Moreover, this approach is in line on what it was found in literature [8,17] and involve a mesh based on the bubble diameter d.

As for the computational domain dimensions, also the mesh changes according to the flow conditions. For HYDRO simulation the mesh is composed by a core region with dimensions of $3d \times 3d$ with uniformly sized square elements of $d/16 \times d/16$ followed by a transition mesh from the core to the walls at which elements measure $d/8 \times d/8$. For the MHD simulations, a mesh near the walls is added to ensure 7 divisions in the MHD boundary layers, as can be observed in Fig. 2. The mesh elements dimension has been defined through a mesh sensitivity study that can be found in Ref. [9]. For the cases with higher magnetic field ($\boldsymbol{B_0} \geq 1$ T), the cell dimension in the core region is $d/24 \times d/24$ to ensure a better resolution near the bubble surface. All the grids have been generated with SALOME. More details about the mesh are reported in Table 2.

Concerning the discretization schemes, the Crank–Nicolson scheme was used with a blend factor of 0.9 for the temporal term, while the second order Gauss linearUpwind was employed for the convection term. The cellMDLimited Gauss linear with a blend factor of 0.333 was used for the gradient terms while for all the other terms the Gauss discretization with linear interpolation of variables was applied. For the surface normal gradients, the non-orthogonal correction was employed.

Regarding the algebraic solvers, the only distinction that was done between HYDRO and MHD simulations concerns the pressure field. The GAMG solver with DIC smoother was used for pressure in the HYDRO simulations while the PCG solver with DIC preconditioner was employed in the MHD ones. This differentiation has been made since it has been noticed by the authors that the GAMG solver is computationally faster than the PCG one; however, its use in the MHD simulations seems to be not suitable due to issues with numerical instability. For the electric potential, it is good practice to use the same linear solver as for the pressure [32]; thus, PCG with DIC preconditioner was used. For the velocity, the PBiCGStab with DILU preconditioner was employed and the isoAlpha reconstruction scheme was used in all simulations for the liquid/gas interface-tracking. Concerning the PIMPLE cycle, 1 nOuterCorrectors and 3 nCorrectors were imposed.

The simulation time-step varies from 10^{-5} s to 10^{-7} s and was estimated following the criterion found in Ref. [17] based on the convective (t_{conv}), viscous (t_{visc}) and surface tension (t_{surf}) characteristic times, with the addition of t_M which is a time-step depending on the magnetic damping time τ_M [32]:

$$\Delta t = \min\left\{t_{conv}, t_{visc}, t_{surf}, t_M\right\} \tag{13}$$

$$t_{conv} = Co\left(\frac{u}{\Delta x} + \frac{v}{\Delta x} + \frac{w}{\Delta x}\right)^{-1} \tag{14}$$

$$t_{visc} = Co\frac{1}{6}\frac{\rho_l \Delta x^2}{\mu} \tag{15}$$

$$t_{surf} = \frac{Co}{2}\sqrt{\frac{\rho_l + \rho_g}{\pi} \cdot Eo \cdot \Delta x^3} \tag{16}$$

$$t_M = Co\left(\frac{u}{\Delta x} + \frac{2}{\tau_M} + \frac{v}{\Delta x^2}\right)^{-1} \tag{17}$$

In the equations, Co is the Courant number, imposed at 0.8, Δx is the minimum computational cell dimension, u, v and w are, respectively, the x, y and z velocity components and, finally, ρ_l and ρ_g are the liquid and gas densities. The results and the characteristic dimensionless parameters of all the simulation performed with mIF are collected in Table 4. As mentioned by Mori et al. [10], all the bubbles analyzed fall within the laminar–turbulent transition region, spanning a Reynolds number range of 10^3–10^4 (refer to Table 4). As an initial approach, we performed the hydrodynamic cases using a laminar model and found quite good agreement, as shown in Table 5, with both the Mori experimental data and the Mendelson formula (Eq. (18)), which is widely used to estimate the bubble terminal velocity u_T in the hydrodynamic regime. Based on this, and considering that the magnetic field tends to "laminarize" the flow by increasing the laminar–turbulent transition range [31], we conducted all the MHD simulations using a laminar model.

$$u_T = \sqrt{\frac{2\gamma}{\rho_l d} + \frac{gd}{2}} \tag{18}$$

The results provided by mIF are in agreement with the experimental data with a maximum discrepancy of approximately 26%. It should be noted that the highest discrepancies from the experimental result occur for the bubbles with the smallest diameter. It was observed that in this particular case, in absence of magnetic field, the experimental values show a significant difference from the bubble terminal velocity values evaluated with the Mendelson formula (Eq. (18)), as confirmed by Table 5. This disparity is likely attributed to the perturbations in the measurement system, mostly for smallest bubbles as shown by

Table 3
Physical properties of mercury and nitrogen [17]. The magnetic permeability used for the mixture Hg/N_2 is that of vacuum.

Property [unit] (symbol)	Mercury	*Nitrogen*
Surface tension coefficient [$N\,m^{-1}$] (γ)	0.4865	
Density [$kg\,m^{-3}$] (ρ)	1.35×10^4	1.17
Electrical conductivity [$S\,m^{-1}$] (σ)	1.02×10^6	1.0×10^{-15}
Dynamic viscosity [Pa s] (μ)	1.50×10^{-3}	1.77×10^{-5}

Mori et al. in fig. 9 [10], concerning the motion field of the metal surrounding the bubble. These disturbances could potentially affect measurements even when the magnetic field is applied.

Other uncertainties might stem from the initial shape of the bubble. As detailed in the original paper [10], creating a perfectly spherical bubble and accurately measuring its diameter and rising velocity in an opaque medium like mercury is particularly challenging. The bubbles were generated by injecting nitrogen through a nozzle, with their diameter estimated based on the nitrogen flow rate and the bubble generation rate measured using an electrical triple probe system, which also measured bubble rising velocity. The authors performed multiple experiments using the same nitrogen flow rate, achieving up to 30% accuracy in velocity measurements due to variations in bubble shape and irregular motion. More details about the bubbles' shape and motion from mIF can be found in Section 4.2. Additionally, the relative error between mIF results and experimental data increases with the magnetic field. This may be due to the thinning MHD boundary layers around the bubble as the magnetic field strengthens, making them difficult to resolve with a uniform mesh. Considering the uncertainties in measuring velocity and the bubble's initial shape and diameter, the authors consider the validation results to be satisfactory.

A comparison of mIF and Zhang & Ni [8] results with the experimental data of Mori et al. [10] is done in Table 6 for the bubble with the largest diameter. It can be observed that both codes have the same error magnitude, except for the case at 1.5 T. The difference of error magnitude between the two codes in this last case, could be associated to the different mesh strategy used in the two studies. The AMR technique used by Zhang & Ni respect to a uniform mesh could provide better resolution of the MHD boundary layer whose importance on bubble motion may grow with increasing interaction parameter N, which in the present case is 8.57. In general, mIF underestimates the velocity respect to the experimental value and, on the contrary, the Zhang & Ni [8] code overestimates it. A code to code benchmark of the bubble rising velocity as a function of time, for the case at 0.5 T and $d = 5.6$ mm, is reported in previous author's paper [9].

4. Results analysis

In this section the results of the bubbles with $d = 2.36$ mm and $d = 5.6$ mm, which correspond respectively to Eo = 1.5 and Eo = 8.5, are analyzed. These bubbles are representative of the laminar to turbulent transition region in which the bubble regime of motion changes significantly, with each one illustrating the extreme behaviors within this zone. Specifically, the electrical variable distribution is discussed, as well as their influence on bubbles shapes, trajectories and wakes.

4.1. MHD variables

For this specific benchmark no numerical or experimental data on electrical variables data were available to compare with the results obtained from mIF code. Therefore, this subsection presents an analytical qualitative discussion.

Since the system involves a horizontal magnetic field oriented along the x-axis, and the primary component of the velocity is along the z-axis, an electric field is predominantly induced in the y-direction. As shown by Eq. (12), a net electric current is generated by the electric field and by the interaction of the magnetic field with the velocity. The electric current lines, which primarily lie in the x-y plane, close in a circular path as illustrated Fig. 6(a). Consequently, the electric potential will be almost symmetric with respect to the y-z plane, as observed in Fig. 3.

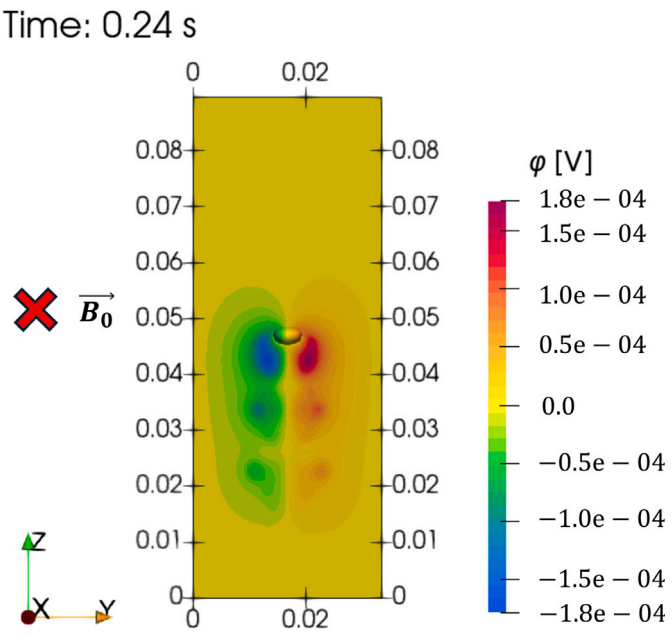

Fig. 3. Quasi-symmetric electric potential x-midplane distribution for the bubble with $d = 5.6$ mm (Eo = 8.5) and $B_0 = 0.5$ T at $t = 0.24$ s.

As discussed also by Corrado & Sato [18], considering that the net current density is mainly directed along the y and z directions, and the applied magnetic field is constant and oriented along the x-axis, the Lorentz force generated is directed along the y and z axes, according to Eq. (19).

$$\boldsymbol{F}_L = \boldsymbol{j} \times \boldsymbol{B_0} = B_0(0, j_z, -j_y) \tag{19}$$

By excluding the contribution of the electric potential to the current density, as done also by Corrado & Sato [18], and expliciting the $\boldsymbol{u} \times \boldsymbol{B_0}$ product into the Lorentz force expression, it is found that the Lorentz force opposes the velocity field, as shown in Eq. (20).

$$\boldsymbol{F}_L = \sigma B_0^2(0, -u_y, -u_z) = -\sigma B_0^2 \boldsymbol{u} \tag{20}$$

Figs. 4 and 5 show the Lorentz force and velocity distribution respectively in y and z directions obtained by mIF code. These results are in agreement with the previous qualitative considerations, demonstrating that in both directions, a positive Lorentz force corresponds to a negative velocity field, and viceversa. As a result, the Lorentz force acts as a damping force, reducing the bubble rise velocity, a phenomenon commonly referred to as the magnetic field braking effect. It is worth noting that the Lorentz force behavior is different from what expected (according to Eq. (20)) near the bubble surface, because is not anymore opposite to the velocity field, as can be seen in Fig. 6(b). This is due to the abrupt change in electrical conductivity from a high value (mercury) to a low value (nitrogen), which leads to a sharp electric potential gradient near the surface, as shown in Fig. 3, where the electric potential isolines exhibit a pronounced curvature upon entering the bubble. This indicates that the electric potential term in Ohm's Law (Eq. (12)) cannot be neglected when deriving Eq. (20) in these region as mentioned above. This, in turn, leads to the deviation in electric current shown in Fig. 6(a), which subsequently affects the Lorentz force, as illustrated in Fig. 6(b). The qualitative relationship between the electric currents and the Lorentz force is evident, particularly in the inversion

Table 4
Results of the validation. The symbols $U_{T,ex}$ and $U_{T,mIF}$ refer, respectively, to the experimental value in [10] and the mIF results. The Reynolds number is evaluated with mIF terminal velocity.

B_0 (T)	d (mm)	Ha	Eo	Re	N	$U_{T,ex}$ (mm/s)	$U_{T,mIF}$ (mm/s)	$E(U_T)$ (%)
0.0	2.36	0	1.5	4400	0	189	207	9.5
0.0	3.87	0	4.0	6600	0	192	189	−1.6
0.0	5.60	0	8.5	10 200	0	202	203	0.5
0.5	2.36	31	1.5	4000	0.24	199	187	−6.0
0.5	3.87	50	4.0	6050	0.42	184	174	−5.4
0.5	5.60	73	8.5	8670	0.62	163	172	5.5
1.0	2.36	62	1.5	3330	1.13	202	157	−22.3
1.0	5.60	146	8.5	6750	3.15	140	134	−4.3
1.5	2.36	93	1.5	2800	3.04	177	132	−25.4
1.5	5.60	219	8.5	5600	8.57	127	111	−12.6

Table 5
Comparison between mIF outcomes for hydrodynamic simulation, Mendelson formula (Eq. (18)) and Mori experimental data [10]. The symbols $U_{T,ex}$, $U_{T,mIF}$ and $U_{T,M}$ refer, respectively, to the experimental values in [10], the mIF results and the analytical evaluation with Mendelson formula. The symbols $E(U_{T,ex})$ and $E(U_{T,M})$ refers respectively to the error between our results and the experimental ones, and our outcomes and the Mendelson formula ones.

B_0 (T)	d (mm)	$U_{T,ex}$ (mm/s)	$U_{T,mIF}$ (mm/s)	$E(U_{T,ex})$ (%)	$U_{T,M}$ (mm/s)	$E(U_{T,M})$ (%)
0.0	2.36	189	207	9.5	205	0.9
0.0	3.87	192	189	−1.6	194	−2.5
0.0	5.60	202	203	0.5	201	1.0

Table 6
Results of the validation for d = 5.6 mm (Eo = 8.5). The symbols $U_{T,ex}$, $U_{T,num}$ and $U_{T,mIF}$ refer, respectively, to the experimental value in [10], to the numerical value in [8] and the mIF results. Both the relative errors $E(U_T)$ are referred to the numerical data respect to the experimental ones.

B_0 (T)	$U_{T,ex}$ (mm/s)	$U_{T,num}$ (mm/s)	$E(U_T)$ (%)	$U_{T,mIF}$ (mm/s)	$E(U_T)$ (%)
0.0	202	200	−1.0	203	0.5
0.5	163	175	7.3	172	5.5
1.0	140	152	6.3	134	−4.3
1.5	127	130	2.3	111	−12.6

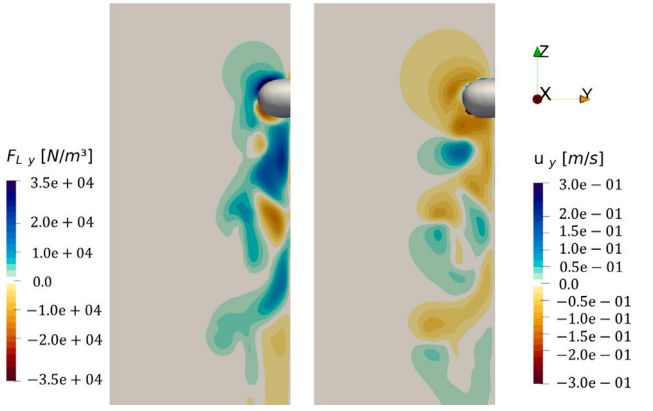

Fig. 4. Distribution of Lorentz force (left) and velocity (right) components in the y-direction, in the x-midplane, for the bubble with d = 5.6 mm (Eo = 8.5) and B_0 = 0.5 T.

of the sign of the z-component of the Lorentz force (blue region near the bubble), which is due to the inversion of the y-component of the electric current density. This confirms the qualitative relationship between the electric currents and the Lorentz force expressed by Eq. (19).

4.2. Bubbles shape and trajectory

The numerical results, concerning bubble shapes and trajectories, presented in this section have been compared mostly with Mori et al. [10] experimental results and with numerical works found in literature [8,18,23]. It is worth mentioning that, in the experiment presented by Mori et al. shapes, velocities and bubble trajectories were estimated

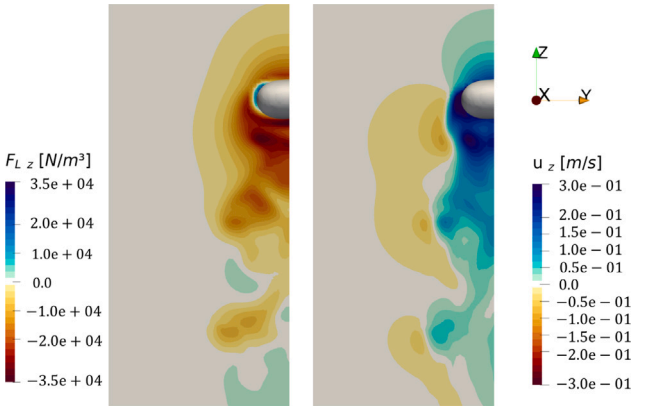

Fig. 5. Distribution of Lorentz force (left) and velocity (right) components in the z-direction, in the x-midplane for the bubble with d = 5.6 mm (Eo = 8.5) and B_0 = 0.5 T.

by a statistical elaboration of the signals obtained from an electrical triple probe [10]. The probe system consisted of three electrodes positioned at different locations in the upper part of the channel, along with one electrode in the generation nozzle. By measuring the time difference between the signal generated by the nozzle electrode and those from the upper electrode(s), Mori et al. were able to determine the bubble rising time and position, allowing the evaluation of velocity, shape and trajectory of the bubbles. The reliability of both the measurement system and of the statistical analysis were demonstrated by Mori et al. comparing the experimental results obtained under hydrodynamic conditions with the Mendelson formula [15] and theoretical considerations on shapes and trajectories by Sawi [33] and Moore [34], which are independent of the material. The bubble rise velocities, measured in hydrodynamic conditions, were used to evaluate the bubble drag coefficients. These results indicate that the bubble behavior in mercury, for the range of diameters investigated, is transitional, falling between the spherical bubble regime, where the drag coefficient is inversely proportional to the bubble Reynolds number, and the spherical cap bubble regime, where the drag coefficient remains constant [10]. In this transitional region, asymmetries in the bubble shape, along with unsteady vortex shedding, cause the bubble to exhibit a spiraling or zig-zagging motion. This kind of path instability can be explained considering that any loss of symmetry in the shape, in the plane

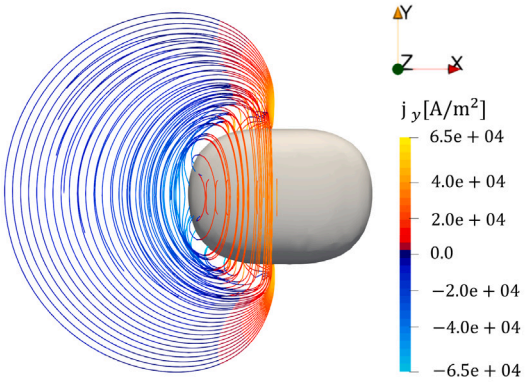

(a) Top view of current density streamlines around the bubble surface. The colors represent the current density directed along the y-axis.

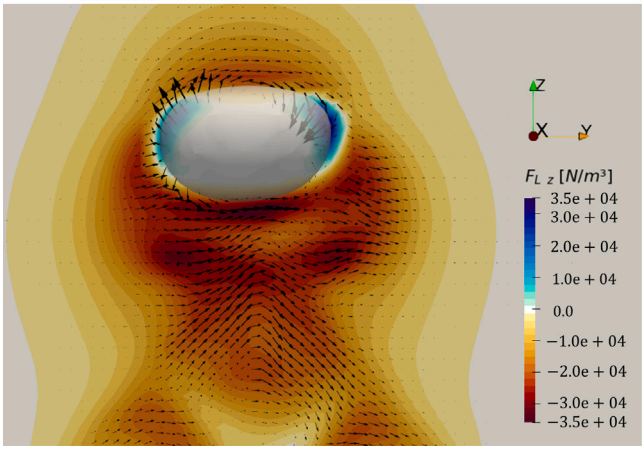

(b) Lorentz force z-component distribution in the Z-Y bubble midplane with current density vectors in black.

Fig. 6. Current density streamlines (a) around the bubble surface and current density vectors (b) with z-component Lorentz force distribution in the x-midplane.

perpendicular to gravity, leads to an imbalance of planar forces, which in turn would drive the bubble away from a straight path [35]. This phenomenon is well-known in the literature about bubble dynamics in liquids.

In Tables 7 and 8 the shapes of the bubbles evaluated by mIF, with d = 2.36 mm (Eo = 1.5) and d = 5.6 mm (Eo = 8.5), are shown, respectively, for different magnetic field intensities. Specifically, it is reported the 0.5 volume fraction isosurface snapshot at t = 0.2 s for each bubble and including views from the top and both sides.

Concerning the small bubble (Eo = 1.5), the flat shape observable for all the transient evaluated by the simulation in hydrodynamic conditions (B_0 = 0 T), as can be seen in Fig. 7, is in agreement with the experimental results obtained by Mori et al. [10].

It can be observed in Fig. 7 and in Table 7 that with the introduction of the magnetic field and its increase from 0.5 to 1.5 T, the bubble shape becomes more spherical. The same behavior has been observed by Corrado & Sato [18] for a bubble with Eo = 2.44. This can be explained with the action of the Lorentz force, whose value increases with B_0. In the z-direction, the Lorentz force primarily suppresses the bubble vertical elongation (Fig. 5, left), while in the y-direction, it inhibits the lateral expansion at the bubble uppermost region (Fig. 4, left). The effect of the magnetic field is observed also on the bubble trajectory, as shown in Fig. 8. Without magnetic field, the bubble has a spiral motion as evaluated by the mIF results and confirmed by

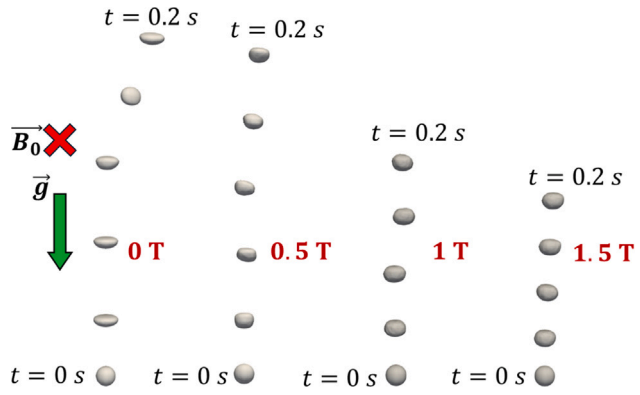

Fig. 7. Bubble of d = 2.36 mm (Eo = 1.5) during the simulation transient of 0.2 s for different magnetic fields.

Table 7
Shape of d = 2.36 (Eo = 1.5) mm bubble at t = 0.2 s.

B_0 (T)	0.0	0.5	1.0	1.5
Y-X view	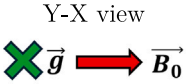			
Z-X view	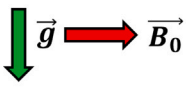			
Z-Y view				

the Mori et al. [10] experiment. The spiral pattern in hydrodynamic conditions is visible but with less emphasis respect to the MHD case because it occurs later in time. Indeed, the hydrodynamic trajectory was calculated for a total of 0.45 s, however, for the sake of consistency, this graph displays results up to 0.25 s, just like in the MHD case. With the magnetic field, the electromagnetic force mainly acts in the y and z directions, reducing the intensity of the velocity components along these axes, as discussed in Section 4.1. As a result, the Lorentz force in these directions causes respectively a decrease in the bubble's movement along the y-axis, resulting in a smaller spiral trajectory radius compared to the hydrodynamic case, as well as a reduction in the vertical path due to the slowing effect of the z-component of the Lorentz force, as shown in Fig. 8. Indeed, as can be seen in Fig. 7, as the magnetic field strengthens, the bubble spiral motion is reduced and the trajectory becomes more linear. According to Mori et al. [10], the decrease in the trajectory radius under MHD conditions, compared to the hydrodynamic case, leads to an acceleration in the bubble's rise that overcomes the vertical braking effect of the magnetic field, resulting in a higher rising velocity in MHD conditions than in the hydrodynamic case. However, the results obtained with mIF suggest that the vertical braking effect dominates the acceleration experienced by the bubble in suppressing the lateral velocity components, leading to a smaller rising velocity in the MHD case compared to the hydrodynamic one. This inconsistency is verified only for the smallest bubble, but as already explained in Section 3, analyzing the results obtained by mIF in the hydrodynamic regime and comparing them with the Mendelson formula results, it may be an issue related to the perturbations in the experiment measurement system.

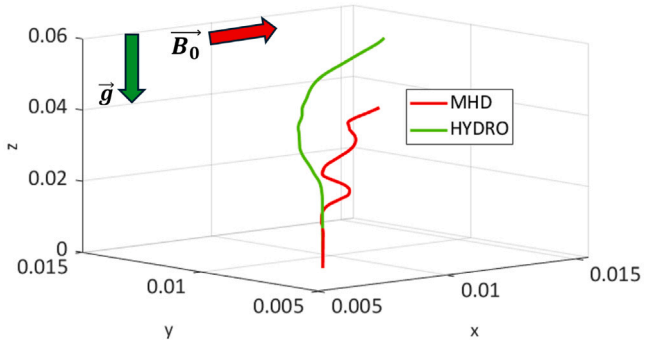

(a) Comparison between hydrodynamic and MHD centroid trajectory for bubble with $d = 2.36$ mm (Eo = 1.5) and $B_0 = 0.5$ T, evaluated by mIF code for a 0.25 s transient.

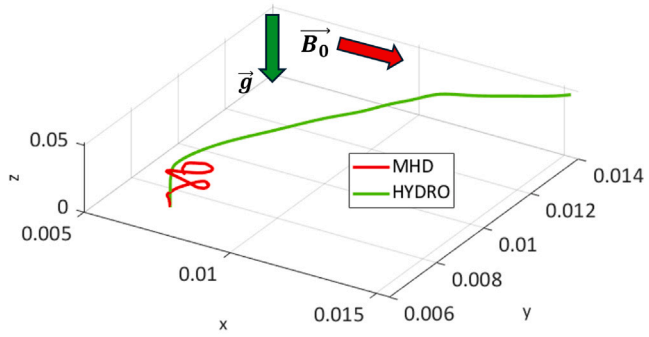

(b) View of the same bubble trajectories from a different point of view.

Fig. 8. Bubble trajectory with and without magnetic field from different views for Eo = 1.5.

Since in the bubble transition region from laminar to turbulent the behavior changes significantly, all the consideration made for the small bubble (Eo = 1.5) cannot be applied to the large one (Eo = 8.5). Indeed, without magnetic field, the bubble shape with Eo = 8.5 does not remain flat during the whole transient, as in the previous case, but becomes wobbling (the large bubble shape during the simulation transient is reported in fig. 7 in the previous authors' paper [9]). Infact, the flat shaped part of the bubble alternates between the upper and lower surfaces, creating an oscillating shape behavior. The wobbling shape experienced by the bubble without magnetic field is associated with the 3D zig-zag motion that was found also in Mori et al. [10] and that can be observed in Fig. 9. With a magnetic field of 0.5 T, the bubble shape becomes elongated in the magnetic field direction, as observed in Table 8 and also in the numerical simulations performed by Pan & Ni [23]. This elongation along magnetic field lines is due to the distribution of the Lorentz force near the bubble surface. As can be observed in Fig. 5, the z component of the electromagnetic force has a positive direction along the bubble side and a negative one on the top part, forcing the bubble to assume a flat shape. In the other hand, the y component of the Lorentz force, presented in Fig. 4 acts mainly to compress the top part of the bubble. For the conservation of mass, the bubble is forced to expand in the direction in which the Lorentz force is not generated, which is the one parallel to the magnetic field. Moreover, the Lorentz force action results in a transition from a 3D zig-zag movement to a nearly zig-zag planar (2D) motion as illustrated in Fig. 9 and confirmed by Mori et al. [10]. This pattern causes a more regular oscillatory motion of the bubble shape during the transient respect to the one in the hydrodynamic case, as observed in author's previous paper [9]. This oscillatory motion is reflected also in the bubble velocity plot that is reported in fig. 8 of author's previous paper [9].

For magnetic fields higher than 0.5 T, the bubble shape becomes irregular. No literature references were found that could be used to compare the findings presented for this specific Eo number and magnetic field conditions. Although Zhang & Ni [8] performed the same simulations, they did not present or comment on bubble shapes for this specific case. The issue could be related to the MHD boundary layer thinning as the magnetic field strength increases. It is worth noting that for Eo = 1.5 and same magnetic field intensities, the bubble shape does not exhibit the same surface irregularities. This difference can be explained by the fact that as the Eo number increases, gravitational forces dominate over surface tension ones, causing the bubble surface to deform. This occurs because the surface tension, which typically acts to minimize the bubble free surface, maintaining its shape spherical, is hardly able to counteract the gravitational forces. As a result, the bubble with Eo = 8.5 deforms more significantly than the bubble with Eo = 1.5. Due to the deformable nature of the bubble, it is challenging to establish a priori a relationship between the boundary layer thickness, bubble dimensions, and the Ha number which increase with both bubble size and magnetic field strength. In this context, depending on the magnetic field strength, bubble orientation, and shape, the boundary layer thickness may vary locally, making it dependent on the local dimensions of the bubble whose shape changes over time. This is in contrast with the uniform boundary layer behavior observed for Hartmann boundary layers in square channels [31], whose thickness depends on a characteristic length that does not change in time and in space. Furthermore, the Lorentz force should be considered in the force balance involving gravitational and surface tension forces since it plays a crucial role in determining the bubble shape as observed in the Eo = 1.5 case.

Table 8
Shape of $d = 5.6$ mm (Eo = 8.5) bubble at $t = 0.2$ s.

$\boldsymbol{B_0}$ (T)	0.0	0.5	1.0	1.5
Y-X view	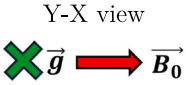			
Z-X view	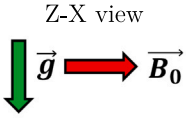			
Z-Y view	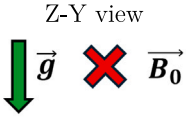			

4.3. Bubbles wake

From Mori et al. experiment [10], it was not possible to visualize the wakes structures behind the bubbles due to the mercury opaqueness. Therefore, in this section, the results of mIF code will be qualitatively discussed following mainly theoretical considerations.

In Tables 9 and 10 the vortex structures corresponding to the bubbles with diameters of $d = 2.36$ mm and $d = 5.6$ mm, respectively, are presented for various magnetic field intensities. The swirling structures are visualized using Q-criterion isosurfaces, specifically for $Q = 100$. In both cases, it can be observed that as the strength of the magnetic field intensifies, there is a corresponding increase in the suppression of vortex structures aligned perpendicularly to it. Conversely, the vortices that are aligned with the magnetic field tend to diffuse and extend along its lines as the field strength increases. The elongation of the wake structures, with their axis aligned along the magnetic field lines, is a consequence of the Lorentz force action on the kinetic energy. In this case, the vortex moves with a velocity perpendicular to the magnetic field, and the interaction between them generates a current.

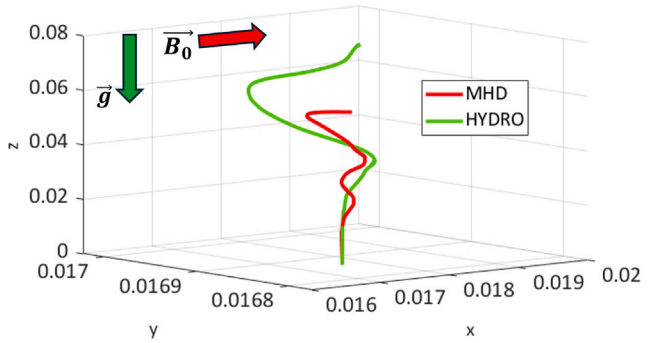

(a) Comparison between hydrodynamic and MHD centroid trajectory for bubble with $d = 5.6$ mm (Eo = 8.5) and $B_0 = 0.5$ T, evaluated by mIF code for a 0.25 s transient.

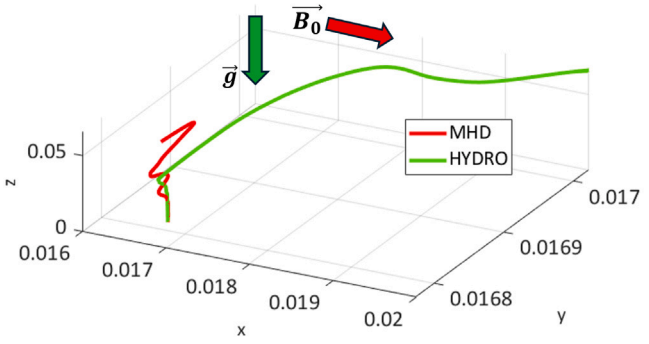

(b) View of the same bubble trajectories from a different point of view.

Fig. 9. Bubble trajectory with and without magnetic field from different views for Eo = 8.5.

This current interacts with the magnetic field, producing a Lorentz force that opposes the vortex's velocity, thereby accelerating the neighboring fluid elements [31]. As a result, the vortex elongates along the magnetic field lines while its rotational motion is decreased. Nevertheless, the angular momentum of the rotating fluid volume stays constant. This process of vortex elongation differs from hydrodynamic vortex stretching, where the vortex diameter decreases and the conservation of angular momentum leads to an increase in rotational speed. In contrast, here, the vortex diameter remains constant, and its volume increases. The conservation of angular momentum causes the vortex motion to slow down [31,36]. Thus, the magnetic field induces the anisotropic diffusion of the bubble wake vortices, meaning the vortices spread differently depending on their alignment with the magnetic field according to Lorentz force action. This effect is further enhanced by the vortex decay times, which differ depending on the vortex orientation respect to the magnetic field [31]. Indeed, the wake structures parallel with the magnetic field have a slower decay time compared to those that are perpendicular, which explains their continued presence in the simulation results [31].

5. Conclusions and future works

In this paper, the behavior of nitrogen bubbles rising in liquid mercury under the influence of a horizontal magnetic field (0–1.5 T) has been studied through a custom numerical code, mIF developed and validated by the Nuclear Energy Research Group (NERG) of Sapienza University of Rome. The validation results, partially presented in the previous authors paper [9] and expanded in the present one, are in agreement with theoretical treatments, experimental and numerical data found in literature [8,10,17,18]. The main effects of the magnetic field on the bubble dynamics were analyzed through numerical investigations performed within the laminar to turbulent transition region,

Table 9
Wake of $d = 2.36$ mm (Eo = 1.5) bubble at $t = 0.2$ s.

$\boldsymbol{B_0}$ (T)	0.0	0.5	1.0	1.5
Z-Y view	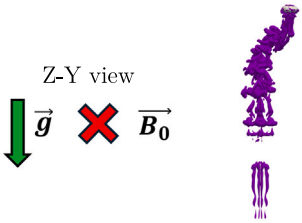			
Z-X view	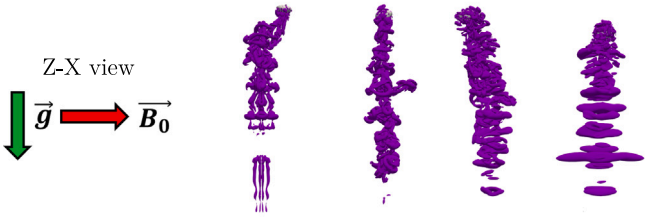			

Table 10
Wake of $d = 5.6$ mm (Eo = 8.5) bubble at $t = 0.2$ s.

$\boldsymbol{B_0}$ (T)	0.0	0.5	1.0	1.5
Z-Y view	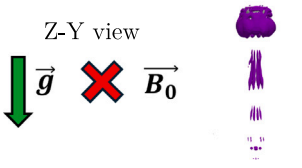			
Z-X view				

considering bubbles with characteristic dimensions representative of the two extremes of the zone (Eo = 1.5, 8.5) which shows very different behavior. Concerning the bubble terminal velocities, the magnetic field lead to a reduction of velocity components perpendicular to the magnetic field through the Lorentz force action, which increases as the magnetic field strengthens. The Lorentz force modifies bubbles trajectories, shapes and wakes. Concerning bubble trajectories and shapes, they depends on balance between gravitational and surface tension forces, expressed by the Eo, which plays a fundamental role in defining bubble regime of motion in the transition region. For the bubble with small Eo number, it was found that with increasing magnetic field the shape becomes more spherical, as also observed by Corrado & Sato [18] for the Lorentz force action, respect to the flat shape shown in hydrodynamic conditions confirmed by Mori experimental results [10]. The Lorentz force modifies also the bubble trajectory, which in this particular case has a spiral motion whose radius is reduced by the magnetic field. For the bubble with large Eo, the wobbling shape without magnetic field leads to a 3D zig-zag motion that becomes planar with the introduction of the magnetic field. This planar pattern causes a oscillatory motion of the bubble. For high magnetic fields ($B_0 > 0.5$), some bubble surface irregularities are observed. They can be caused by a lack of resolution in the MHD boundary layer around the bubble whose thickness should

be reduced by the magnetic field combined with a predominance of gravitational forces over surface tension. In order to solve this aspect, some attempts have been done using the AMR technique but at the current stage its application in miF is hindered by the propagation of numerical errors for different time discretization schemes. The authors aim to develop an AMR technique that can be applied to the MHD equations, and to integrate it into the code. Additionally, they plan to extend the validation by comparing the results from `mIF` with both analytical and experimental data for a LM flow with a free surface, subjected to a constant applied magnetic field, considering both insulating and conductive wall conditions [37,38]. To this end, since `mIF` does not currently include wall modeling, an integration with the `chtMultiRegionFoam` code is necessary to accurately simulate the conditions of LM systems and components under development for fusion reactors. The `chtMultiRegionFoam` code has already been integrated with MHD equations and validated by the authors for MHD single-phase flow simulations [9]. Future work will also include the integration of a helium nucleation model, currently being developed by the NERG group, along with the equations governing the transport of dissolved tritium in a LM, which have already been integrated and validated by the NERG group in `chtMultiRegionFoam` [39].

CRediT authorship contribution statement

Sonia Pignatiello: Writing – review & editing, Writing – original draft, Visualization, Validation, Software, Methodology, Investigation, Formal analysis, Conceptualization. **Simone Siriano:** Writing – review & editing, Visualization, Validation, Software, Methodology, Investigation, Formal analysis. **Alessandro Tassone:** Writing – review & editing, Supervision, Conceptualization.

Declaration of competing interest

The authors declare that they have no known competing financial interests or personal relationships that could have appeared to influence the work reported in this paper.

Acknowledgments

This work has been carried out within the framework of the EUROfusion Consortium, funded by the European Union via the Euratom Research and Training Programme (Grant Agreement No 101052200 — EUROfusion). Views and opinions expressed are however those of the author(s) only and do not necessarily reflect those of the European Union or the European Commission. Neither the European Union nor the European Commission can be held responsible for them.

The computational resources and the related technical support used for this work have been provided by CRESCO /ENEAGRID High Performance Computing infrastructure and its staff [40]. CRESCO/ENEAGRID High Performance Computing infrastructure is funded by ENEA, the Italian National Agency for New Technologies, Energy and Sustainable Economic Development and by Italian and European research programmes, see www.cresco.enea.it/english for information.

During the preparation of this work, the author(s) used the OpenAI GPT language model, commonly known as ChatGPT, in order to improve the clarity and structure of English writing, as well as to assist with formatting tasks. After using this tool/service, the author(s) reviewed and edited the content as needed and take(s) full responsibility for the content of the publication.

Simone Siriano and Alessandro Tassone acknowledge the funding and support of Sapienza University of Rome, Italy through the grant no. RP123188F6A17C66 Progetti di Ricerca Piccoli 2023 - “Nucleation and transport of immiscible gas bubbles within a heavy liquid metal in hydrodynamic and magnetohydrodynamic conditions”

Data availability

Data will be made available on request.

References

[1] L. Batet, J. Fradera, E.M. de les Valls, L. Sedano, Numeric implementation of a nucleation, growth and transport model for helium bubbles in lead–lithium HCLL breeding blanket channels: Theory and code development, Fusion Eng. Des. 86 (4) (2011) 421–428, http://dx.doi.org/10.1016/j.fusengdes.2011.03.074.

[2] M. Kordač, L. Košek, Helium bubble formation in Pb-16Li within the breeding blanket, Fusion Eng. Des. 124 (2017) 700–704, http://dx.doi.org/10.1016/j.fusengdes.2017.05.100.

[3] L. Bühler, C. Mistrangelo, J. Konys, R. Bhattacharyay, Q. Huang, D. Obukhov, S. Smolentsev, M. Utili, Facilities, testing program and modeling needs for studying liquid metal magnetohydrodynamic flows in fusion blankets, Fusion Eng. Des. 100 (2015) 55–64, http://dx.doi.org/10.1016/j.fusengdes.2014.03.078.

[4] J. Roenby, H. Bredmose, H. Jasak, IsoAdvector: Geometric VOF on general meshes, in: J. Nóbrega, H. Jasak (Eds.), OpenFOAM®, Springer, 2019, pp. 281–296, http://dx.doi.org/10.1007/978-3-319-60846-4_21, The 11th OpenFOAM® Workshop ; Conference date: 26-06-2016 Through 30-06-2016.

[5] J. Roenby, H. Bredmose, H. Jasak, A computational method for sharp interface advection, R. Soc. Open Sci. 3 (2016) 160405, http://dx.doi.org/10.1098/rsos.160405.

[6] H. Scheufler, J. Roenby, Accurate and efficient surface reconstruction from volume fraction data on general meshes, J. Comput. Phys. 383 (2019) 1–23, http://dx.doi.org/10.1016/j.jcp.2019.01.009.

[7] S. Siriano, N. Balcázar, A. Tassone, J. Rigola, G. Caruso, Numerical Simulation of High-Density Ratio Bubble Motion with interIsoFoam, Fluids 7 (2022) 152, http://dx.doi.org/10.3390/fluids7050152.

[8] J. Zhang, M.J. Ni, Direct simulation of multi-phase MHD flows on an unstructured cartesian adaptive system, J. Comput. Phys. 270 (2014) 345–365, http://dx.doi.org/10.1016/j.jcp.2014.03.030.

[9] S. Siriano, L. Melchiorri, S. Pignatiello, A. Tassone, A multi-region and a multiphase MHD OpenFOAM solver for fusion reactor analysis, Fusion Eng. Des. 200 (2024) 114216, http://dx.doi.org/10.1016/j.fusengdes.2024.114216.

[10] Y. Mori, K. Hijikata, I. Kuriyama, Experimental Study of Bubble Motion in Mercury With and Without a Magnetic Field, J. Heat Transf. 99 (1977) 404–410, http://dx.doi.org/10.1115/1.3450710.

[11] C. Zhang, S. Eckert, G. Gerbeth, Experimental study of single bubble motion in a liquid metal column exposed to a DC magnetic field, Int. J. Multiph. Flow 31 (2005) http://dx.doi.org/10.1016/j.ijmultiphaseflow.2005.05.001.

[12] Z. Chaojie, Liquid metal flows driven by gas bubbles in a static magnetic field, 2009.

[13] Z.H. Wang, S.D. Wang, X. Meng, M.J. Ni, UDV measurements of single bubble rising in a liquid metal galinstan with a transverse magnetic field, Int. J. Multiph. Flow 94 (2017) http://dx.doi.org/10.1016/j.ijmultiphaseflow.2017.05.001.

[14] T. Richter, O. Keplinger, N. Shevchenko, T. Wondrak, K. Eckert, S. Eckert, S. Odenbach, Single bubble rise in GaInSn in a horizontal magnetic field, Int. J. Multiph. Flow 104 (2018) http://dx.doi.org/10.1016/j.ijmultiphaseflow.2018.03.012.

[15] H.D. Mendelson, The prediction of bubble terminal velocities from wave theory, AIChE J. 13 (1967) 250–253, http://dx.doi.org/10.1002/aic.690130213.

[16] A. Tomiyama, T.S.I.K. Iztok Zun, Drag coefficients of single bubbles under normal and micro gravity conditions, JSME Int. J. Ser. B (1998) http://dx.doi.org/10.1299/jsmeb.41.472.

[17] K. Jin, P. Kumar, S.P. Vanka, B.G. Thomas, Rise of an argon bubble in liquid steel in the presence of a transverse magnetic field, Phys. Fluids 28 (2016) http://dx.doi.org/10.1063/1.4961561.

[18] M. Corrado, Y. Sato, Magnetohydrodynamics Simulation of the Nonlinear Behavior of Single Rising Bubbles in Liquid Metals in the Presence of a Horizontal Magnetic Field, Fluids 7 (2022) http://dx.doi.org/10.3390/fluids7110349.

[19] K. Ueno, M. Higashitani, S. Kamiyama, Study on single bubbles rising in magnetic fluid for small Weber number, J. Magn. Magn. Mater. 149 (1995) http://dx.doi.org/10.1016/0304-8853(95)00348-7.

[20] K. Ueno, T. Nishita, S. Kamiyama, Numerical simulation of deformed single bubbles rising in magnetic fluid, J. Magn. Magn. Mater. 201 (1999) http://dx.doi.org/10.1016/S0304-8853(99)00026-8.

[21] D. Merrouche, K. Mohammedi, I. Belaidi, Coupling the VOF and the MHD models for the simulation of bubble rising in a metallic liquid, Int. J. Mater. Form. 1 (2008) http://dx.doi.org/10.1007/s12289-008-0173-2.

[22] Y. Shibasaki, K. Ueno, T. Tagawa, Computation of a rising bubble in an enclosure filled with liquid metal under vertical magnetic fields, ISIJ Int. 50 (2010) http://dx.doi.org/10.2355/isijinternational.50.363.

[23] Y. Pan, J. Zhang, Z.-H. Wang, M.-J. Ni, Development of MHD solver based on an adaptive mesh refinement technique, Fusion Eng. Des. 87 (2012) 630–633, http://dx.doi.org/10.1016/j.fusengdes.2012.01.040.

[24] S. Schwarz, J. Fröhlich, Numerical study of single bubble motion in liquid metal exposed to a longitudinal magnetic field, Int. J. Multiph. Flow 62 (2014) http://dx.doi.org/10.1016/j.ijmultiphaseflow.2014.02.012.
[25] X.H. Tian, W.Y. Shi, T. Tang, L. Feng, Influence of vertical static magnetic field on behavior of rising single bubble in a conductive fluid, ISIJ Int. 56 (2016) 195–204, http://dx.doi.org/10.2355/isijinternational.ISIJINT-2015-493.
[26] A. Blishchik, M. van der Lans, S. Kenjereš, An extensive numerical benchmark of the various magnetohydrodynamic flows, Int. J. Heat Fluid Flow 90 (2021) 108800, http://dx.doi.org/10.1016/j.ijheatfluidflow.2021.108800.
[27] T.F. Flint, M.C. Smith, P. Shanthraj, Magneto-hydrodynamics of multi-phase flows in heterogeneous systems with large property gradients, Sci. Rep. 11 (2021) http://dx.doi.org/10.1038/s41598-021-97177-8.
[28] C. Hirt, B. Nichols, Volume of fluid (VOF) method for the dynamics of free boundaries, J. Comput. Phys. 39 (1) (1981) 201–225, http://dx.doi.org/10.1016/0021-9991(81)90145-5.
[29] J.U. Brackbill, D.B. Kothe, C. Zemach, A continuum method for modeling surface tension, J. Comput. Phys. 100 (1992) 335–354, http://dx.doi.org/10.1016/0021-9991(92)90240-Y.
[30] M.-J. Ni, R. Munipalli, P. Huang, N.B. Morley, M.A. Abdou, A current density conservative scheme for incompressible MHD flows at a low magnetic Reynolds number. Part II: On an arbitrary collocated mesh, J. Comput. Phys. 227 (2007) 205–228, http://dx.doi.org/10.1016/j.jcp.2007.07.023.
[31] U. Müller, L. Bühler, Magnetofluiddynamics in Channels and Containers, Springer Berlin Heidelberg, Berlin, Heidelberg, 2001, http://dx.doi.org/10.1007/978-3-662-04405-6,
[32] E.M.D. les Valls, Development of a Simulation Tool for MHD Flows Under Nuclear Fusion Conditions (Ph.D. thesis), Universitat Politècnica de Catalunya, 2011.
[33] M.E. Sawi, Distorted gas bubbles at large Reynolds number, J. Fluid Mech. 62 (1) (1974) 163–183, http://dx.doi.org/10.1017/S0022112074000620.
[34] D.W. Moore, The velocity of rise of distorted gas bubbles in a liquid of small viscosity, J. Fluid Mech. 23 (4) (1965) 749–766, http://dx.doi.org/10.1017/S0022112065001660.
[35] M.K. Tripathi, K.C. Sahu, R. Govindarajan, Dynamics of an initially spherical bubble rising in quiescent liquid, Nat. Commun. 6 (6268) (2015) http://dx.doi.org/10.1038/ncomms7268.
[36] P.A. Davidson, Magnetic damping of jets and vortices, J. Fluid Mech. 299 (1995) 153–186, http://dx.doi.org/10.1017/S0022112095003466.
[37] A.Y. Shishko, A theoretical study of steady film flows in a coplanar magnetic field, Magnetohydrodynamics 28 (1992) 170–181.
[38] M. Hvasta, E. Kolemen, A. Fisher, H. Ji, Demonstrating electromagnetic control of free-surface, liquid-metal flows relevant to fusion reactors, Nucl. Fusion 58 (1) (2017) 016022, http://dx.doi.org/10.1088/1741-4326/aa9344.
[39] F. Hattab, S. Siriano, F. Giannetti, An OpenFOAM multi-region solver for tritium transport modeling in fusion systems, Fusion Eng. Des. 202 (2024) 114362, http://dx.doi.org/10.1016/j.fusengdes.2024.114362.
[40] F. Iannone, F. Ambrosino, G. Bracco, M.D. Rosa, A. Funel, G. Guarnieri, S. Migliori, F. Palombi, G. Ponti, G. Santomauro, P. Procacci, CRESCO ENEA HPC clusters: A working example of a multifabric GPFS Spectrum Scale layout, 2019 Int. Conf. High Perform. Comput. Simul. HPCS 2019 (2019) 1051–1052, http://dx.doi.org/10.1109/HPCS48598.2019.9188135.